Euler-Equation-Based Drag Minimization of Unconventional Aircraft Configurations

Hugo Gagnon[1] and David W. Zingg[2]
University of Toronto, Toronto, Ontario M3H 5T6, Canada

This study investigates the potential of unconventional aircraft transports through numerical optimization. Three distinct configurations are investigated: a box wing, a C-tip blended wing-body, and a braced wing. Each transport is sized for the same regional mission and is subjected to the same optimization strategy based on the Euler equations. The figure of merit is inviscid pressure drag at transonic speed; the nonlinear constraints are lift, pitching moment, and internal volume. The design variables include the section shape and twist distribution of the main lifting surfaces. It is found that the box-wing, C-tip blended-wing-body, and braced-wing configurations investigated here are respectively 34.1%, 36.2%, and 40.3% more efficient than a similarly optimized conventional tube-and-wing configuration. Each optimization revealed in one way or another the importance of accounting for flow nonlinearity during the early stages of unconventional aircraft design. For the blended wing-body, the C-tip does not appear to provide a drag benefit over a purely vertical winglet, presumably as a result of the compressibility effects prevalent in the C opening. For the braced wing, compressibility effects also lead to a curious result, where the supporting strut finds itself carrying negative lift at the optimum.

Nomenclature

b	span [m]
C_p	pressure coefficient

[1] Ph.D. Candidate, Institute for Aerospace Studies. AIAA Student Member.
[2] Professor and Director, Institute for Aerospace Studies, Tier 1 Canada Research Chair in Computational Aerodynamics and Environmentally Friendly Aircraft Design, J. Armand Bombardier Foundation Chair in Aerospace Flight. AIAA Associate Fellow.

D	drag [N]
e	span efficiency
L	lift [N]
n	normal force (section) [m]
q_∞	freestream dynamic pressure [N/m^2]
W	weight [N]
x, y, z	chordwise, spanwise, and vertical coordinates [m]
α	angle of attack [deg]

I. Introduction

Fuel economy is now more than ever of paramount importance for the aeronautical industry [1]. Not only do fuel efficient aircraft cost less to operate, but they also produce less emissions responsible for climate change. One way to reduce fuel burn is to reduce drag, since thrust equals drag at steady flight. Current aircraft are, however, remarkably efficient; thus, step changes in drag reduction are unlikely unless radically-new unconventional technologies are considered [2].

The two main drag components acting on a typical aircraft are viscous and induced drag. Induced drag, defined as the kinetic energy added to the wake per unit distance traveled, is an inviscid phenomenon experienced by lifting wings of finite span. It constitutes roughly 40% of the total drag at cruise and up to a staggering 90% of the total drag during ascent [3]. Reducing this form of drag is therefore highly rewarding and is the motivation behind this study.

Munk [4] was the first to identify the elliptical lift distribution as the one producing the minimum induced drag among all planar wings of the same span and lift. His results were based on the well-known lifting-line theory of Prandtl [5], which was later refined by Cone [6] for lifting systems with "spanwise camber". These and other ideas culminated in the vortex-lattice method and its use in numerical optimization to find the minimum induced drag of arbitrary nonplanar lifting systems [7].

While nonplanar wings may produce less induced drag compared to planar wings of the same span and lift, aircraft are not built on the basis of induced drag with fixed span and lift. To account for viscosity,

structures, and other effects, several authors have recently coupled their aerodynamic analyses with other models of varying degrees of fidelity; see, for example, [8–12]. While insightful, these studies are nonetheless limited by the linear aerodynamic assumption.

Van Dam [13] demonstrated that higher span efficiencies than those predicted by linear theory are possible for planar crescent-moon-shaped wings since such wings shed a nonplanar wake at an angle of attack. Smith [14] and Smith and Kroo [15] confirmed that beneficial nonlinear wing-wake interaction can indeed lead to lower induced-drag values, provided that the shape of the rolled-up, force-free wake is accurately modeled. More recently, Liersch *et al.* [16] concluded that higher-order effects such as induced lift explain why a spanwise cambered elliptical wing produces less induced drag than the same unfolded wing.

Another important yet often overlooked nonlinear effect influencing induced drag is compressibility. Even with the Prandtl-Glauert correction, incompressible-flow models at higher Mach numbers fail to predict the correct optimal lift distribution of simple planar objects such as swept-back wings [14]. For nonplanar wings in transonic flow, the incompressible assumption is not only inaccurate but also unreliable.

The necessity of incorporating high-fidelity models in the investigation and assessment of unconventional aircraft is being increasingly recognized [17–19]. The difficulty, of course, is to use such models effectively as design tools. In the case of models based on computational fluid dynamics (CFD), aerodynamic shape optimization (ASO) is invaluable, since it has the potential to exploit the nonlinearity of the flow without human intervention beyond problem setup [20].

Applications of CFD-based ASO to wing design have up until recently largely focused on the Euler equations [21–28]. Contrary to circulation-distribution and panel methods, the Euler equations do not require the user to prescribe the starting location and shape of the wake. Compressibility effects are also inherently captured. On the downside, the influence of viscosity on induced drag is ignored; in particular, side-edge flow separation at the wingtips may not match the true viscous flow [14].

This study uses ASO based on the Euler equations to investigate the potential for induced-drag reduction of four transonic aircraft configurations. Consistency is emphasized; each configuration is sized for the same mission and is optimized using the same geometry control system as well as the same flow solver and optimizer. Stability, structures, and other such considerations are purposefully excluded from the analyses, so as to isolate the role of flow nonlinearity on induced drag.

This study does not attempt to provide a definite answer as to which unconventional aircraft configuration is superior to the other, nor does it attempt to find the "real world" optimum for each configuration. Such questions can only be answered through multi-disciplinary, multi-objective, and multi-point optimizations involving high-fidelity viscous flow models. Instead, this study focuses on the influence of flow nonlinearity on the aerodynamic design and induced drag of unconventional aircraft.

Section II of this paper describes the methodology used to carry the optimizations. Specifically, Section II A reviews each aircraft configuration in the context of previous work, Section II B overviews the optimization problem common to all four configurations, and Section II C gives some details on the grids used throughout the optimizations. The results of those optimizations are presented in Section III, where Sections III A to III D are each assigned one configuration. Finally, Section IV summarizes the main findings and concludes the paper.

II. Methodology

A. Concept Selection

Many unconventional aircraft transports have been proposed throughout the history of aviation. Each transport represents a compromise between competing objectives and constraints for a given mission. Lange [29], for example, reviews a flatbed, a multibody, and a wing-in-ground-effect configuration for very large cargo aircraft.

The configurations investigated here are targeted at the medium-haul, 100-passenger market segment. They are: a tube-and-wing, a box wing, a C-tip blended wing-body, and a braced wing. Relative to the tube-and-wing, each unconventional configuration has the potential to substantially reduce induced drag. While other configurations such as the D8 aircraft of Drela [30] are equally promising in that regard, here priority is given to those configurations with larger vertical extents for their more interesting nonplanar wake structure.

Figure 1 depicts the initial geometry of all four transports. Their planform is based on already existing designs, which are scaled for the present study to ensure that the fuselages contain enough room to house the passenger compartments (also visible in Fig. 1). Note that the fuselages and engines shown here are not included in the flow analyses of the ASO problems,[1] although their weights are considered, as explained in

[1] Including the fuselage alongside a wing in a shape optimization problem introduces a host of difficulties [22]; in fact, retaining the

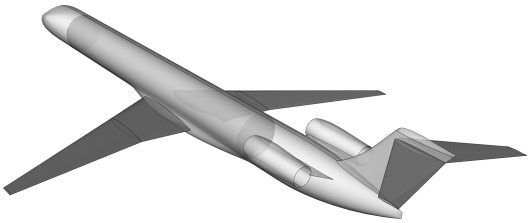

(a) tube-and-wing

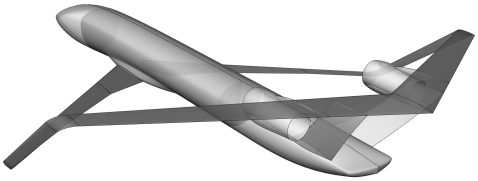

(b) box wing

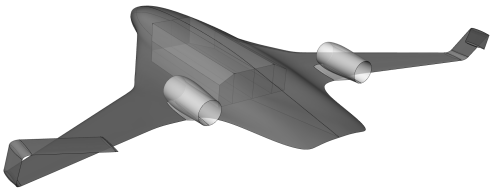

(c) blended wing-body

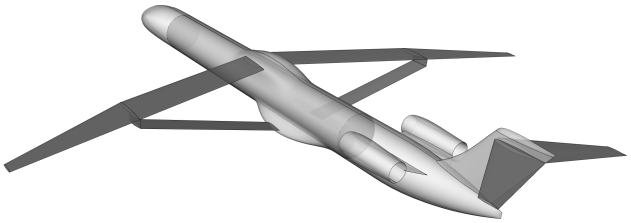

(d) braced wing

Fig. 1 Regional transports.

Section II B.

With the exception of the bracing strut in Fig. 1d, the wings of each transport are generated exclusively from NASA's integral supercritical airfoils [31]. These airfoils are characterized by a large leading-edge radius, thus providing reasonable low-speed performance, and a reduced curvature over the middle region of the upper surface, thus delaying the shock and, ultimately, drag rise. They thus provide an excellent starting point for the ASO problems since here the freestream Mach number is fixed at 0.78 for all cases, in agreement with the reported cruising speeds of most regional jet transports.

---

design intent (quality) of the fairing at a wing-body junction is arguably the most challenging task of any aerodynamic optimizer.

Table 1 Dimensions and key data

	Tube-and-wing	Box wing	Blended wing-body	Braced wing
Dimensions [m]				
Wing span	26.30	26.30	30.73	34.15
Overall length	38.79	34.31	21.10	38.79
Overall height	6.15	6.60	3.81	6.02
Wetted area [m^2]				
Wing	134.23	179.81	478.58	182.69
Fuselage	282.91	285.73	–	291.72
Horizontal tail	30.43	–	–	30.43
Vertical tail	21.10	30.76	–	21.10
Total	468.66	496.30	478.58	525.92
Weight and balance[a]				
W/q_∞ [m^2]	38.16	39.18	40.10	39.84
Center of gravity[b] [m]	4.44	10.34	12.39	4.05

[a] At the beginning of the cruise segment.

[b] Measured from the leading edge of the foremost wing segment at the symmetry plane.

Wing segments (the darker surfaces separated by thin black lines in Fig. 1) are each generated by sweeping a root airfoil or a blend of a root and tip airfoils along a trajectory curve [32]. The airfoils are used as is, with the exception of the centerbody of the blended wing-body, for which the thickness-to-chord ratio of the root airfoil is increased by scaling it in the vertical direction. Also, for the blended wing-body only, the blending between the root and tip airfoils is nonlinear; specifically, the blending is linear from root to midspan and then constant based on the tip airfoil only.

An overview of each transport is given next; refer to Table 1 for more detailed specifications.

1. Tube-and-Wing

The baseline tube-and-wing shown in Fig. 1a is modeled after publicly available information on the Bombardier CRJ1000.[2] The pressurized cabin is designed for a 2-2 seating arrangement and is long enough to seat 104 passengers in economy class.

The main wing is essentially a scaled-up version of the CRJ700 planform: straight leading edge swept back 30 degrees with a root plug ending at 35% semispan. Based on a mix of historical trends and two-dimensional methods as described in Raymer [33], the NASA SC(2)-0614, SC(2)-0412, and SC(2)-0410 airfoils are chosen at the root, kink, and tip sections, respectively. This choice yields satisfactory lift coefficients and internal volume at the expense of small wave-drag penalties.

Rather than trying to replicate the exact winglet of the CRJ1000, the choice is made not to include a winglet on the initial geometry but, as will be discussed in Section III A, the optimizer is given enough freedom to produce one on its own.

2. Box Wing

For a fixed span, the box wing is most appealing from the perspective of induced drag: in theory, if the two wings of a biplane are infinitely separated, and each one carries half the lift of a monoplane of the same span, then the induced drag is halved. If, further, a biplane is joined at its tips by end plates, then reductions on the order of 40% are predicted for vertical-gap-to-span ratios of about 0.3 [5]. These results should also hold for swept wings in transonic flow by virtue of Munk's stagger theorem [4].

In practice, several difficulties were uncovered in the high-subsonic regime by Lange *et al.* [34]. Chief among these was wing divergence encountered well below the target flutter speed. This problem was also well recognized by Frediani [35], whose solution was to mount the rear wings on two vertical fins separated by a maximum horizontal distance. Although the models employed in the present study do not account for aeroelasticity, the two fins are nevertheless positioned aft of the fuselage as shown on Fig. 1b, though like the fuselage they are excluded from the aerodynamic analyses.

The initial airfoil selection is of little importance since the flow curvature induced by the neighboring

[2] http://commercialaircraft.bombardier.com/en/crj.html [retrieved 1 May 2015]

wings calls for highly customized airfoils [36]. Here, most the of wing loop is generated from the NASA SC(2)-0410 airfoil, with the exception of the vertical tip fins, which are generated from the NASA SC(2)-0010 symmetric airfoil.

3. Blended Wing-Body

Unlike most unconventional transports, the blended wing-body has been the subject of many ASO studies based on flow models as accurate as the Reynolds-averaged Navier-Stokes equations [37–41]. This popularity is undoubtedly due to its geometric simplicity (in its simplest form the blended wing-body is really just a wing with nonlinearly varying taper).

The blended wing-body shown in Fig. 1c is inspired from the released press on the X-48C demonstrator. Unlike the X-48C, it features C-tip extensions, thus providing longitudinal and directional control and stability on top of mitigating induced drag [3].

The nose bullet, intended for increased cockpit visibility, somewhat complicates surface generation. Indeed, the challenging task of fitting the necessary volume inside a compact yet smooth blended wing-body of this size might very well explain its usual application to very large transports [42, 43]. Here, a 2-4-2 cabin layout is assumed to ensure ride quality, with the cargo bays and fuel tanks located outboard.

An airfoil stack arising from the combination of a (modified) NASA SC(2)-0010 airfoil at the root and an (unmodified) NASA SC(2)-0410 airfoil at the tip is fitted in a single sweep to generate a C^2 continuous outer mold line. No initial twist is prescribed; therefore, the initial configuration generates barely any lift. However, as will be pointed out in Section III C, the optimizer easily remedies this situation by pitching up the centerbody by only a few degrees.

4. Braced Wing

Braced wings can be traced back to the early days of aviation, but it is Pfenninger [44] who revived the concept for high-speed transports. The design motivation is to use a strut, or a system of trusses, to alleviate wing bending-torsion. This in turn allows for higher aspect-ratio wings with lower thickness-to-chord ratios. The thinner wings have less transonic wave drag, permitting the wings to unsweep thus favoring natural laminar flow.

Understandably, aerostructural considerations are particularly important in the design of braced wings.

Elements of multidisciplinary analysis and optimization have thus been incorporated in recent studies [45–50]. Although some of these studies involve CFD, none involve CFD-based ASO.

As per the general guidelines of Bhatia *et al.* [48], the strut of the braced wing shown in Fig. 1d intersects the wing at 60% semispan. The span is chosen to be 1.3 times that of the tube-and-wing, leading to an aspect ratio of roughly 16.4; in comparison, values of 16.0, 16.4, and 19.55 are reported in [50], [44], and [49], respectively. As in [50] the strut is unswept, and as in [45] it has a vertical portion aimed at reducing compressibility effects at the wing-strut junction.

The wing is generated from the NASA SC(2)-0412 airfoil at the root and the NASA SC(2)-0410 airfoil at the tip, while the strut is entirely generated from the NACA 64A-010 symmetric airfoil. Just like the previous three transports, all wing segments are initially untwisted and those intersecting the fuselage, i.e. the symmetry plane, have zero angle of incidence.

B. Optimization Problem

In order to draw direct comparisons based on absolute drag, it is important that all four transports be optimized in a consistent manner. To begin with, each transport must be able to perform the same mission, which consists of carrying 100 passengers and 3 crew members over 926 km ($\approx$ 500 nm) at Mach 0.78 and an altitude of 10.5 km ($\approx$ 35,000 ft). Since only single-point optimizations are conducted here, the most critical point of the cruise segment is picked, i.e. at the beginning, where the required lift is maximum.

As stated in Section I, "real world" applications normally require multiple flight conditions to be included within the same optimization problem. This is especially true for regional jets, since it is not uncommon for such transports to spend a short period of time at cruise relative to climb and descent. Multi-point optimizations are, however, beyond the scope of this work (as are structural deflections and other important effects). Here, the focus is on nonlinear aerodynamics not easily captured with panel or other simplified methods.

For each case the sum of induced and wave drag, i.e. inviscid pressure drag, is minimized using the same gradient-based aerodynamic optimizer. The main building blocks of the optimizer are described and validated in Hicken and Zingg [51]. In particular, it solves the Euler equations on multi-block structured grids and computes the gradients of the flow-dependent functionals using the discrete-adjoint method.

Surface deformation is handled by a geometry control system based on two-level free-form and axial

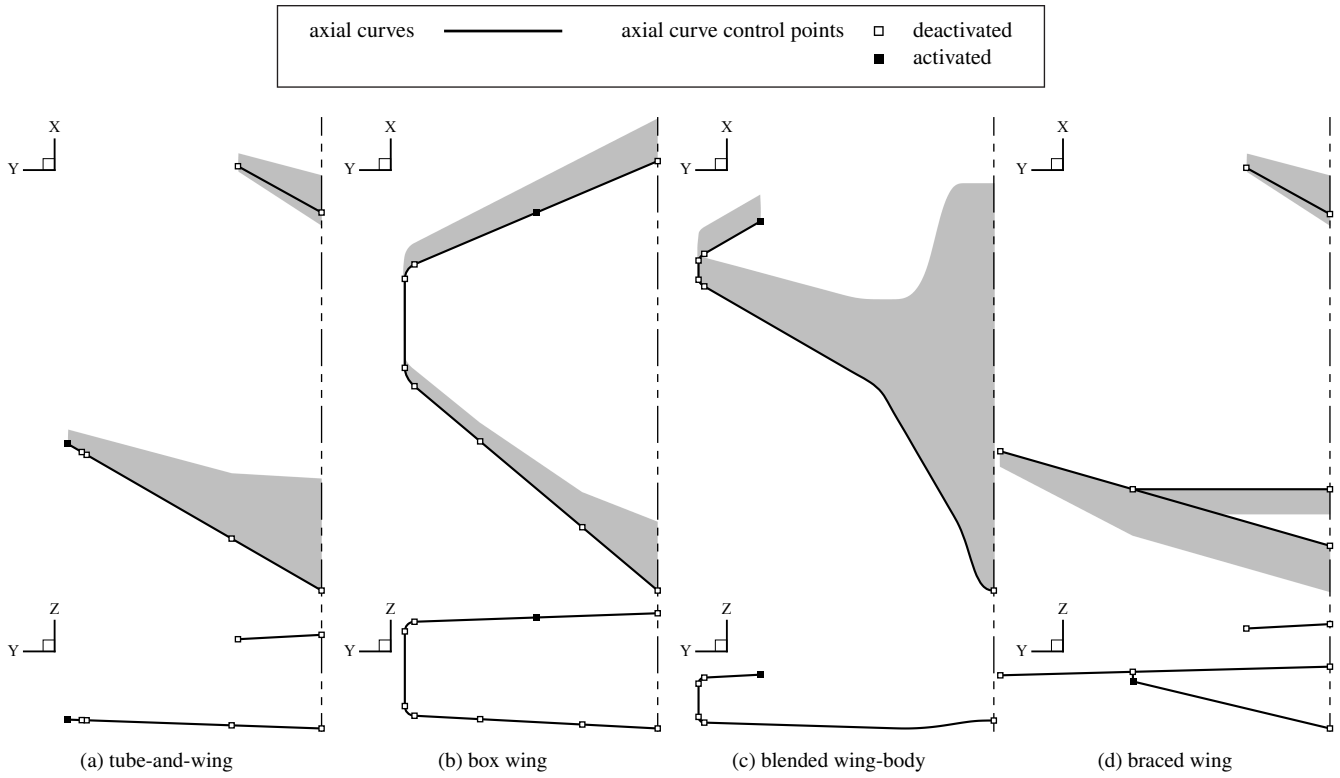

Fig. 2 Geometry parameterizations.

deformation [52]. Using this technique, so-called axial curves handle variations in sweep, span, and dihedral, while free-form-deformation (FFD) volumes handle variations in twist, taper, and section shape. Both the axial curves and the FFD volumes are modeled with B-splines.

As shown in Fig. 2, in general one axial curve is used per wing segment, irrespective of its length and function. Doing so allows one to retain the design intent of the wing systems, as opposed to using a single continuous axial curve to parameterize, for example, the entire box wing. This approach also greatly simplifies problem setup, since the trajectory curves used to generate the wing segments can then be reused as axial curves. Note that only the end control points of the axial curves are shown on Fig. 2, except for the top wing of the box wing, for which the middle control point is also shown.

Some of the axial-curve control-point coordinates are activated with the goal of exploring the design space of each configuration. Depending on the configuration at hand, an attempt is made to do so in a manner that is sensible both from an aerodynamic and a structural point of view. For example, for the conventional wing only, a winglet is allowed to grow (to help it compete with the unconventional designs), but the winglet's taper is heavily restricted (to help reduce the surface area). In general, because there is no structural model

involved, neither wing span, nor wing sweep, nor wing taper is allowed to vary during any of the optimizations.

Note that the FFD volumes (not shown in Fig. 2) achieve variations in twist and section shape relative to the axial curves. Therefore, the placement of the axial curves relative to the wing segments matters. For example, if an axial curve is placed at the leading edge of a wing segment then that wing segment will twist about its leading edge.

The approach to isolating induced drag is to eliminate wave drag by enabling section shape changes. By further allowing twist changes, the optimizer should be able to recover span efficiencies equal to or greater than 1 by optimally loading all lifting surfaces. The twist design variables include the angle of incidence of the wing sections at the symmetry plane. For maximum flexibility the freestream angle of attack is also allowed to vary between -5 and 5 degrees. The intent is to promote design space exploration while limiting the development of overly pitched airfoils.

Enabling detailed section shape control to eliminate wave drag drastically increases the number of geometric design variables. This is because here each spanwise FFD-volume cross section responsible for shape control is defined with 10 chordwise and 2 vertical rows of control points, which translates to 20 section design variables per cross section. While it is recommended to use at least 4 FFD-volume cross sections (80 section design variables) per wing segment, this number may be overly conservative in certain cases.

To prevent the wings from becoming excessively thin as a result of the optimizations, their internal volume is forced to maintain at least 95% of their initial value. Additionally, the vertical scaling factors responsible for section shape control are constrained to a lower bound of 0.6. Thus, for example, a wing section that is initially 10% thick cannot become less than 6% thick. This is with the exception of the cross sections covering the centerbody of the blended wing-body, for which, given the cabin height requirement, the lower bound is set to 0.95.

Two nonlinear constraints other than the internal volume are imposed to respectively satisfy the lift and trim requirements at the beginning of cruise. Linear constraints are also imposed but are specific to each configuration. For example, more often than not twist is linearly interpolated between the two tip cross sections of an FFD volume assigned to a given wing segment, a measure that reduces the development of wavy surfaces in the spanwise direction and that fortunately has a minimal impact on drag.

To estimate the aircraft weights, and therefore the required lift at the specified speed and altitude, a low-

fidelity model based on wetted area is used [33]. In this model, each major aircraft component is assigned a single weight per unit area, and that same value is used for all configurations. For example, the weight of the tube-and-wing is reflected by the wetted areas of its "wing", "horizontal tail", "vertical tail", and "fuselage" components. The same goes for the box-wing and braced-wing configurations. In the case of the blended wing-body, only the "wing" component is used for the lack of a better weight estimate for the embedded fuselage. Although of limited accuracy, this approach at least ensures that each aircraft is sized according to the same technology levels. The values used in this work are calibrated against the reported operating empty weight of the CRJ1000. The calibration assumes predetermined weights for the propulsion, system, operational, payload, and fuel load groups, all taken as percentages of the takeoff gross weight of an aircraft of the same class [33].

The wing segments used to perform the flow analyses of the tube-and-wing, box-wing, and braced-wing configurations include the wing portions that are normally buried inside the fuselage. This approach tends to overpredict the actual lift of the full aircraft, hence for those configurations the gross weight is multiplied by a factor of 1.05.

Note that the aircraft weights are used for the sole purpose of calculating the target lift at the beginning of each optimization. During the optimizations, the effect of varying twist and section shape on the surface area and therefore the weight is not accounted for. Even if it were, the variations in weight are small, since, as discussed in the previous paragraphs, the design parameters responsible for span, sweep, and taper are in general fixed. The lower bounds on section shape control and the internal volume constraint further limit variations in wetted areas.

The center of gravity of the tube-and-wing is set at 25% of its mean aerodynamic chord (MAC), whereas the centers of gravity of the unconventional aircraft are calculated based on their component-weighted centroids. The longitudinal position of the centers of gravity is considered a design variable, with an upper bound of 35% MAC for the tube-and-wing. For the unconventional aircraft a margin of 5% of the fuselage length is used in order to account for their greater overall uncertainty in wing planform and overall design.

C. Baseline Grids

Predicting drag through CFD in the context of ASO is not without difficulty. Not only does artificial dissipation affect the solution, but also the thin shape of wings makes it difficult to accurately resolve pressure gradients with reasonable mesh sizes [53]. Even though wake-plane analyses are typically more accurate than surface-based predictions [54], this trend diminishes with increasing mesh density [23]. The approach taken here, therefore, is to use coarse grids to run the optimizations and to use fine grids to retrieve grid-converged lift and drag values, either before or after the optimizations have taken place. Based on the authors' experience, see also [55], this approach yields similar relative results compared to optimizations conducted on finer grids, even though the absolute drag values can differ significantly on the finer grids. Of course, using coarse grids for the optimizations has the added benefit of significantly reducing computational cost. A breakdown of the CPU time required to evaluate the objective function and gradient components on grids comprising millions of nodes is given in [51].

Some statistics of the baseline grids are listed in Table 2. The final spacings will vary slightly as a result of mesh movement. However, the off-wall spacings at the wing roots will remain on the order of 10^{-3} root-chord units. The fine grids are obtained by refining, in parameter space, the B-spline block mappings responsible for mesh movement [51], thus ensuring that the surface nodes coincide with the underlying geometry. The refined grids are used to produce all the plots and figures of Section III.

The smaller off-wall spacings of the tube-and-wing relative to the other configurations are due to the wingtip treatment. Node clustering is used to ensure that the optimizer catches the right (subtle) aerodynamic trade-offs when morphing a winglet. Also, taper is applied to the baseline surface grid at the tip, which further reduces the mesh cell sizes there by a factor of 3 or so.

III. Results

The results of the drag minimizations summarized in Table 3 are now discussed for each configuration. Since lift and span are constrained in all cases, the drag minimizations are equivalent to span-efficiency maximizations. Recall that the span efficiency of a lifting system can be computed without resorting to reference areas:

$$e = \frac{(L/q_\infty)^2}{\pi b^2 (D/q_\infty)}. \tag{1}$$

Table 2 Grid data in root-chord units

	Block	Node	Spacing ($\times 10^{-3}$)		Far-field distance[b]
			Off-wall	Wall[a]	
Tube-and-wing					
Coarse	126	3,466,800	0.0989	11.60	25.0
Fine	2544	97,712,968	0.0278	3.83	25.0
Box wing					
Coarse	96	3,395,562	0.3524	15.30	24.4
Fine	2354	98,001,819	0.1021	4.99	24.4
Blended wing-body					
Coarse	234	1,540,000	0.2459	5.74	25.0
Fine	2391	91,652,311	0.0434	1.47	25.0
Braced wing					
Coarse	248	4,436,424	0.3107	27.74	20.9
Fine	2191	95,023,706	0.1170	10.06	20.9

[a] Average surface spacing $\equiv \sqrt{S/N_{\text{surf}}}$, where S is the surface area and N_{surf} is the number of nodes on the surface.

[b] Minimum distance to the far-field boundary.

Table 3 Summary of the drag minimizations

	e	L/D	L/q_∞ [m^2]	D/q_∞ [m^2]	
Tube-and-wing	1.026	54.3	40.71	0.7491	
Box wing	1.479	80.3	39.69	0.4939	(-34.1%)
Blended wing-body	1.207	86.1	41.20	0.4782	(-36.2%)
Braced wing	0.993	89.9	40.22	0.4472	(-40.3%)

Recall also that this metric is only relevant for lifting systems of the same span and lift; therefore, although it provides a useful benchmark against linear theory, it is not intended to compare the relative performance of the configurations.

As described in Section II B, the analyses do not account for viscous drag and the optimizations do not include the fuselage, engines, and vertical tail of the configurations. It is therefore important to take the L/D and thus the percentage improvements in this context. The wetted areas are, however, more or less the same before and after the optimizations as a result of fixing span, sweep, and taper, which also prevents the optimizer from exploiting the planform shapes in favor of even lower inviscid drag values.

Euler-equation-based solutions are often characterized by unrealistic pressure recovery regions due to the inability of the Euler equations to model flow separation [56]. Despite this limitation, the pressure-coefficient and wing profiles of each configuration are still reported in this section. The intent is to give the reader insight into the physics as opposed to suggesting what the profiles should look like on real aircraft.

The values reported in Table 3 are computed from post-optimization fine-grid flow analyses. Consequently, the lift values reported here differ from the target lift values used for the optimizations. This can be seen by comparing the W/q_∞ and L/q_∞ values in Tables 1 and 3, respectively. Had the angles of attack been adjusted at the end of the optimizations to recover the target lift values, the drag values would be more or less 6% lower (since the lift values are on average 3% larger than the target values). That being said the absolute drag values are somewhat irrelevant; what matters here is the relative performance of the configurations as reported in the last column of Table 3. Although more work is needed, these performance trends are expected to remain the same should the weight estimates and therefore the target lift values change slightly (as a result of using a different weight model or optimizing at different cruise conditions, for example).

A. Tube-and-Wing Configuration

The initial tube-and-wing configuration is shown on the left-hand side of Fig. 3a. Shocks are clearly visible aft on the inboard wing and outboard close to the leading edge. To remedy this, a total of five axial curves are defined, as shown in Fig. 2a. The first four axial curves are assigned to the wing and are positioned directly on its leading edge, thus ensuring that the latter remains straight regardless of twist, whereas the fifth axial curve is positioned on the quarter-chord curve of the horizontal tail. The axial curves control a total of

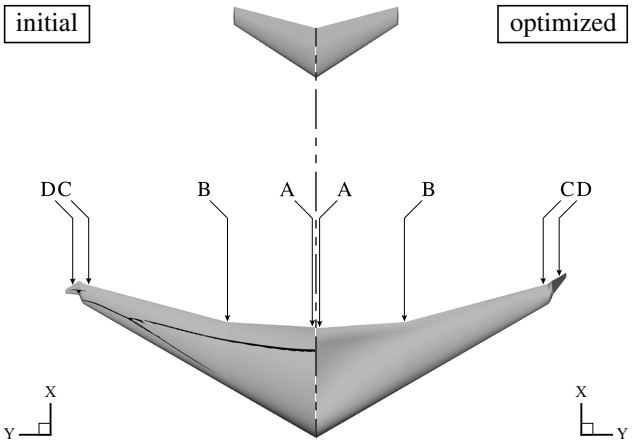

(a) shock surfaces

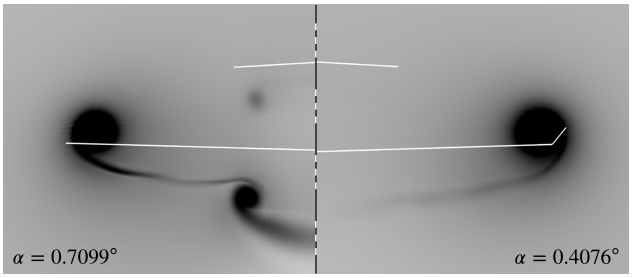

(b) wake structure

Fig. 3 Initial (left) and optimized (right) tube-and-wing configuration.

23 independent FFD-volume cross sections. All cross sections are allowed to twist; however, there are only 7 effective twist design variables since, for any given FFD volume, twist is linearly interpolated between the tip cross sections. Each and every control point forming the 19 cross sections controlling the wing is allowed to scale along its local vertical axis, leading to 380 section design variables (19×20). Finally, the x and z coordinates of the fourth axial curve's outermost control point can vary. The intent is to encourage the optimizer to produce a winglet on its own by controlling the streamwise and vertical extents of the wingtip extension. A smooth wing-winglet transition is ensured by the third axial curve. Note that taper is enforced manually on the winglet at the beginning of the optimization and is therefore not a design variable.

Figure 3a on the right-hand side shows the optimized wing and tail. All shocks are eliminated and, as expected, the optimizer reached the upper bound of the winglet's streamwise and vertical extents. By reshaping the remaining wing segments, the optimizer also managed to achieve a span efficiency greater than 1 despite the trim constraint. This efficiency gain is reflected by the smoother structure of the wake on the right-hand side of Fig. 3b. Note that the wake structures shown in this paper are produced from views located

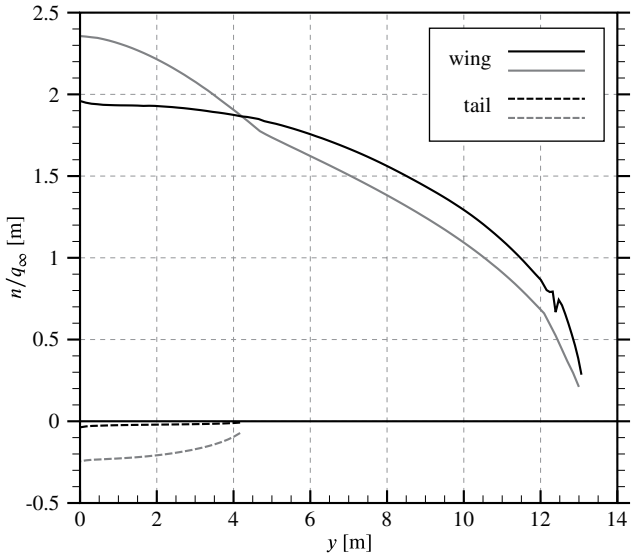

Fig. 4 Initial (gray) and optimized (black) normal-force distributions of the tube-and-wing configuration.

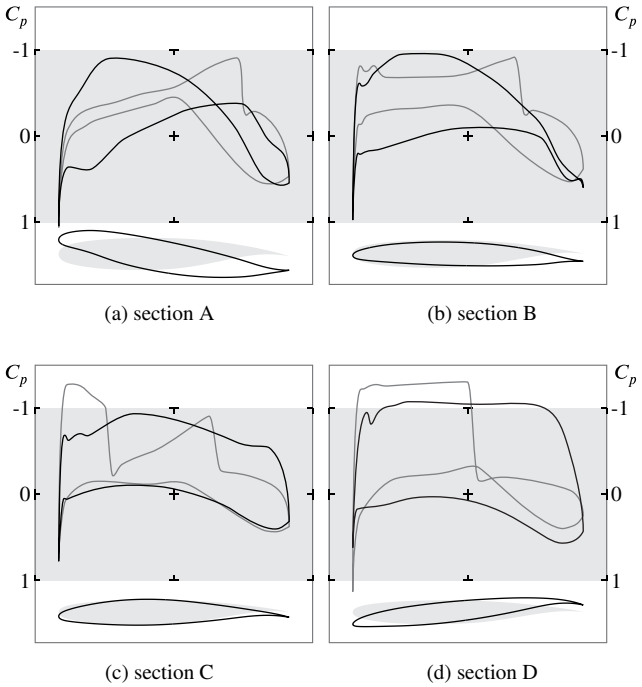

Fig. 5 Initial (gray) and optimized (black) pressure-coefficient profiles of the tube-and-wing configuration. Sections A–D correspond to those of Fig. 3a.

80 m downstream of the configurations and perpendicular to the reported angles of attack.

Compared with the initial configuration, the spanwise normal-force distribution of the optimized configuration is much more elliptical; see Fig. 4. The winglet thus experiences significant side-forces, in agreement with the design guidelines of Whitcomb [57]. As for the tail, it is forced to carry some negative lift due to the

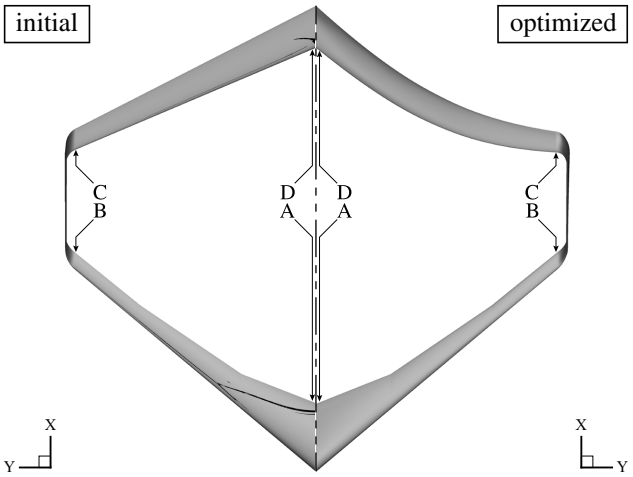

(a) shock surfaces

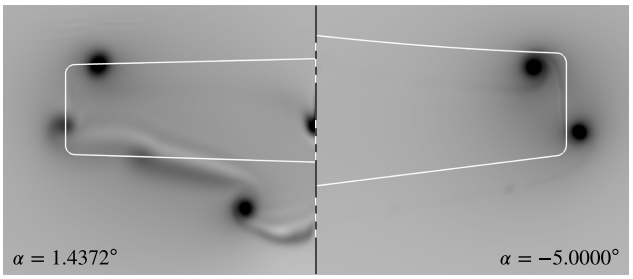

(b) wake structure

Fig. 6 Initial (left) and optimized (right) box-wing configuration.

position of the center of gravity, which in turn forces the optimizer to increase the loading on the wing in order to achieve the required total lift while keeping the force distribution smooth. The optimizer tries to minimize this balancing act by heavily contorting the wing sections, especially at the root (section A) as seen in Fig. 5. The pressure recovery regions are nevertheless much more gentle on the optimized sections, except perhaps on the suction side of the winglet, where the steep pressure gradients would likely cause separation in viscous flow [56]. Of particular interest is the striking resemblance between section D of the optimized winglet and the "typical winglet section" reported by Whitcomb in his seminal 1976 study [57, Fig. 3 on page 19].

For comparison, the same optimization problem was repeated but without the permissible vertical extent (that is, with 1 less degree of freedom), and it was found that the winglet-up configuration produces roughly 3.5% less drag.

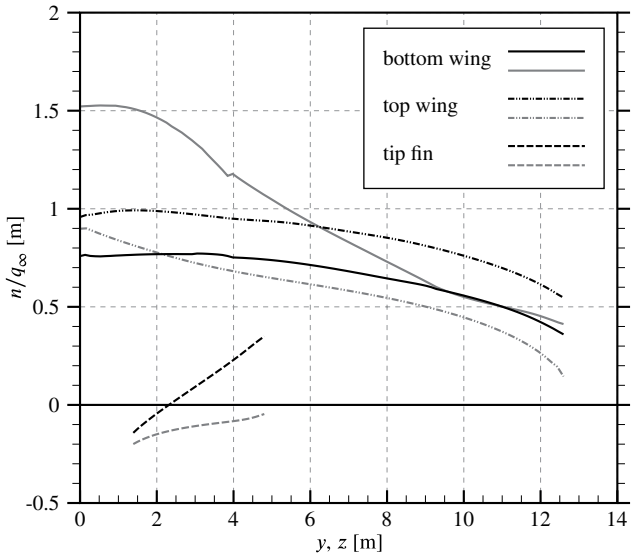

Fig. 7 Initial (gray) and optimized (black) normal-force distributions of the box-wing configuration.

B. Box-Wing Configuration

The initial flow solution of the box-wing configuration is smoother overall than that of the tube-and-wing due its thinner airfoils, with the exception of a strong but thin shock located outboard along the leading edge of the front wing and a localized supersonic bubble at the leading-edge root of the rear wing; see Fig. 6a. Smooth flow gradients are also observed on the inboard portion of the vertical tip fin. To set up the optimization, one axial curve is positioned on the leading edge of each wing segment, including the two corner fillets, for a total of 7 axial curves. In all, there are 26 FFD-volume cross sections, totaling 520 section design variables (26×20). Like the tube-and-wing, all middle cross sections of each FFD volume are linearly interpolated from the tip cross sections; thus, there are only 8 effective twist design variables. Finally, the optimizer is also given some freedom in shaping the planform of the top wing through the middle control point of its axial curve (see Fig. 2b), which is quadratic. Only the x (chordwise) coordinate of that control point is allowed to vary.

By the end of the optimization the optimizer reached the lower bound of that last design variable leading to the nonlinear planform shape shown on the right-hand side of Fig. 6a. As seen in the same figure the optimizer also removed all shocks. It also redistributed the load carried by each wing segment, see Fig. 7, resulting in smooth spanwise and vertical force distributions. The final span efficiency is 1.479; in comparison, according to Frediani [35] the span efficiency of a box wing of height-to-span ratio of 0.2 and no dihedral should be about

1.47. The span efficiencies are thus in excellent agreement. However, it should be noted that the effective height-to-span ratio of the optimized configuration is in fact closer to 0.3 when accounting for the final angle of attack of -5 degrees. This can be seen by comparing the height of the initial and final axial curves on Fig. 6b. Also of particular interest on Fig. 6b is the final wake structure of the optimized configuration, which has its number of vortex cores reduced to two down from four.

By reaching the lower bound of -5 degrees on the angle of attack, the optimizer effectively maximized the vertical distance between the top and bottom wings when looking toward the out-of-plane axis (i.e. the axis perpendicular to the plane passing through both wings). This is expected since for box wings the larger the height-to-span ratio the larger the span efficiency [5]. To investigate the impact of the angle of attack on the solution, the same optimization was set up but without any bound on the angle of attack. Although this second optimization resulted in considerably less drag, it eventually failed at an angle of attack of about -16 degrees. The failure was attributed to mesh movement problems caused by heavy twisting of the wings which is necessary to satisfy the lift and trim constraints. Presumably, if the optimizer could, it would completely realign the freestream along the out-of-plane axis so to maximize span efficiency. Although of academic interest this solution has of course no practical value.

In contrast to the span efficiency, the force distributions shown in Fig. 7 may at first glance appear a little surprising. The optimal force distribution of the box wing is generally shown as the sum of a constant and elliptical lift distributions that is equally carried by the top and bottom wings, joined at their tips by butterfly-shaped side-force distributions [5]. However, as remarked by Kroo [3], what this observation does not account for is that a vortex loop of constant circulation can be superimposed on such a closed system without changing its total lift and drag. This is indeed what is observed in Fig. 7: the force distribution is similar to the one described above, only here it is slightly "shifted" onto the top wing. Given the gradient-based nature of the optimization, this result is likely sensitive to the initial design and flow conditions, i.e. it corresponds to a local optimum.

The remarkable capability of the box wing to adapt its optimal force distribution at virtually no performance cost is confirmed in a recent study by Gagnon and Zingg [58], who also show that when trim, stability, and root-bending moment constraints are included in the optimization problem then a box wing outperforms a tube-and-wing by 17.8% more than when no such constraints are imposed.

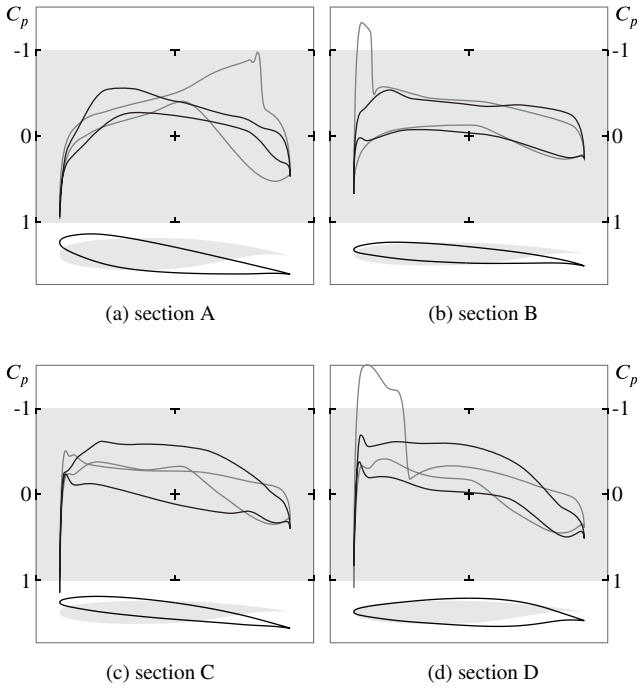

Fig. 8 Initial (gray) and optimized (black) pressure-coefficient profiles of the box-wing configuration. Sections A–D correspond to those of Fig. 6a.

As seen in Fig. 8, the flow field induced by the neighboring wings has a substantial impact on the wing sections. Similar trends to those observed on the joined wing by Wolkovitch [59] are visible. First, whereas the bottom wing is washed-out (the incidence at section B is less than at section A), the bottom wing is washed-in (the incidence at section D is more than at section C). Second, the bottom wing (sections A–B) incorporates more camber than the bottom wing (sections C–D).

C. Blended-Wing-Body Configuration

Inspecting Fig. 9a, the initial blended-wing-body configuration has shocks, both on the outboard wing and in the transonically-stressed flow environment located inside its C-tip extension. For the optimization, a total of 5 axial curves are used, visible in Fig. 2c: one going from the root of the centerbody all the way to the tip, one for the vertical tip fin, one for the horizontal winglet, and two for the smooth corner transitions. All the axial curves are positioned on the leading edge of their respective wing segment. There are a total of 29 FFD-volume cross sections, and section shape control is activated on each one of them, leading to 580 section design variables (29×20). Twist is linearly constrained between the root, midspan, and tip cross sections of the centerbody-outboard segment, and also on the other wing segments between their tip cross sections, for a

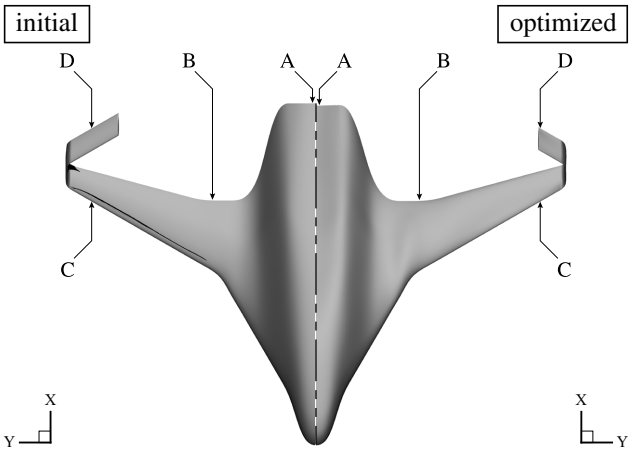

(a) shock surfaces

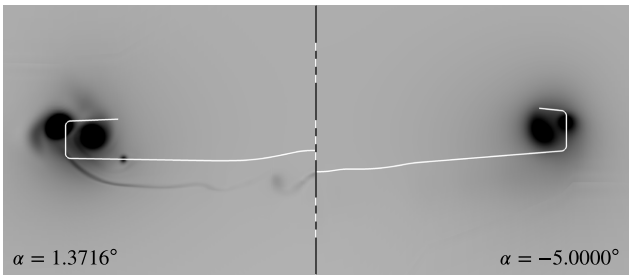

(b) wake structure

Fig. 9 Initial (left) and optimized (right) blended-wing-body configuration.

total of 7 effective twist design variables.

The blended wing-body is, in a sense, doubly unconventional with its C-tip extension. Unlike their planar counterparts, the aerodynamics of C-tip blended wing-bodies have not received much attention in the past; see [60] for a rare exception. Thus, the focus here is on the C-tip extension, more specifically on its top horizontal segment. Originally, both its length and dihedral angle were allowed to vary, but the optimizer invariably tried to eliminate it in favor of a higher vertical winglet, i.e. it wanted to "unfold" the C shape. Another optimization was thus set up, where this time the horizontal segment could only vary in length. As seen from the resulting planform in Fig. 9a, the optimizer still chose to reduce the horizontal segment's length as much as it could, suggesting that for a fixed vertical-gap-to-span ratio, the C-tip is not advantageous — perhaps even disadvantageous — over a purely vertical winglet. Although surprising, a similar conclusion was reached by Verstraeten and Slingerland [8] when comparing optimally-loaded wingletted and C wings based on total drag.

As seen in Fig. 10, the spanwise force distribution on the centerbody of the blended wing-body remains

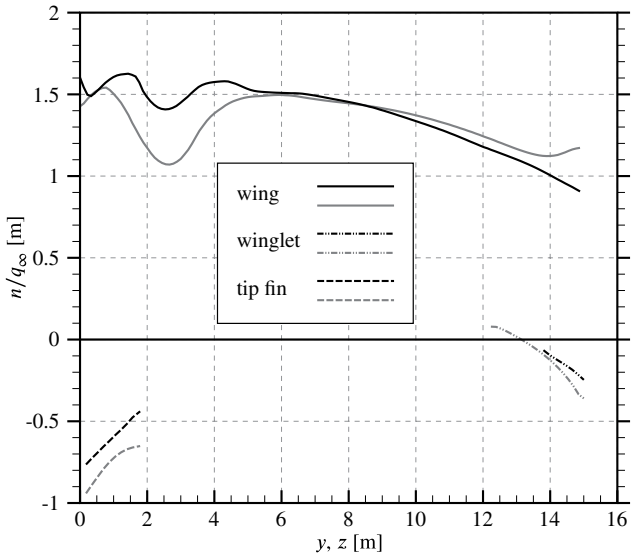

Fig. 10 Initial (gray) and optimized (black) normal-force distributions of the blended-wing-body configuration.

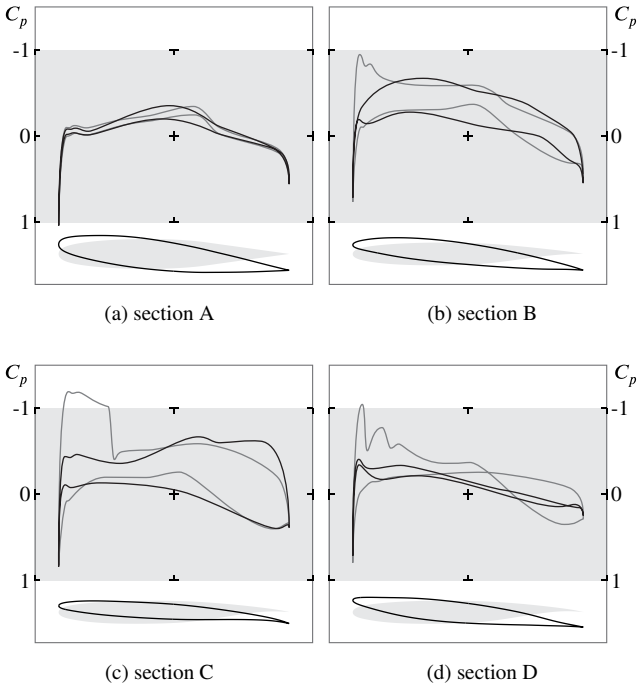

Fig. 11 Initial (gray) and optimized (black) pressure-coefficient profiles of the blended-wing-body configuration. Sections A–D correspond to those of Fig. 9a.

nonmonotonic after the optimization. Similar observations were made by Qin *et al.* [37], who attributed this result to the compressibility effects arising from the lateral disturbances caused by the presence of a highly tapered centerbody. Surprisingly, the horizontal winglet experiences a downward force at optimality, a finding that is however consistent with those of others [3, 8, 61].

Just as interestingly, as seen in Fig. 9b the optimizer partially merged the two tip vortices, thus reducing the kinetic energy lost to the wake and therefore the induced drag. Similar to the box wing it also maximized the vertical distance between the top and bottom wings (i.e. the effective height-to-span ratio) by reaching the lower bound of -5 degrees on the angle of attack. Relative to this value the incidence angle of the centerbody's root section reached 2.1 degrees, thus favoring a reasonable deck angle at cruise. As seen in Fig. 11 the incidence angles at the tip (sections C and D) are also small relative to the freestream, and similar to the box wing the thickness-to-chord ratios are larger at the top (section D) than at the bottom (section C).

D. Braced-Wing Configuration

Shocks reside on most top surfaces of the initial braced wing despite its thin sections and relatively small wing loading. Axial curves are assigned to wing segments in a similar fashion as in the previous three cases, yielding 5 effective twist and 340 section design variables. The strut, being a purely structural member, is not allowed to twist and has limited freedom in section shape changes. The extent of its vertical portion, however, is allowed to change by plus or minus 0.1 root-chord units. The intent is to help the optimizer relieve the flow passing through the wing-strut opening. Finally, with the exception of the section located at the wing-strut junction, taper is activated on all 11 FFD-volume cross sections covering the main wing segments. Because the axial curves are positioned on the wing's trailing edge, the latter is ensured to remain straight as taper is varied.

The flow on the optimized shape is remarkably well-behaved, as evidenced by the absence of shocks and the much weaker trailing vortices on the right-hand sides of Fig. 12. Notice how the initial kink at 60% semispan disappears, blended by a smooth leading edge.

Even more interesting is the fact that the span efficiency of the full system is very close to unity despite the strut carrying a negative (downward) force distribution over the entirety of its span; see Fig.13. However counterintuitive it may seem, this solution is optimal: the overall lift distribution, i.e. when considering the lift contribution from all surfaces, including those of the tail, is indeed very close to elliptical.

To investigate whether the download on the strut is due to a lack of geometric flexibility, the same optimization problem was repeated but with the twist of the strut allowed to vary. The new solution (not shown here) remained almost identical. This intriguing result may be explained by the transonic and compressible

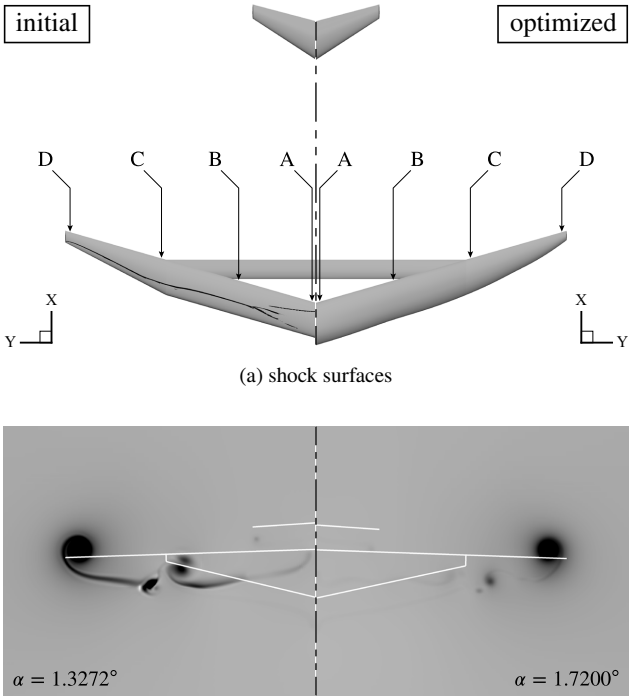

(a) shock surfaces

(b) wake structure

Fig. 12 Initial (left) and optimized (right) braced-wing configuration.

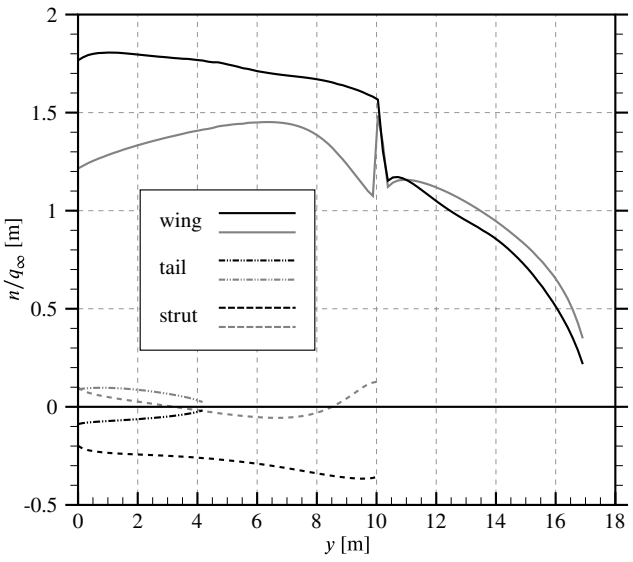

Fig. 13 Initial (gray) and optimized (black) normal-force distributions of the braced-wing configuration.

nature of the flow. Indeed, it was found by Ko *et al.* [62] that the wing-strut opening effectively acts as a nozzle, choking the flow at the minimum area between the top surface of the strut and the bottom surface of the wing. Having nowhere else to go, the flow spills under the strut at higher velocities and thus lower pressures thereby creating the downward force. Here the optimizer mitigated this nozzle effect by increasing

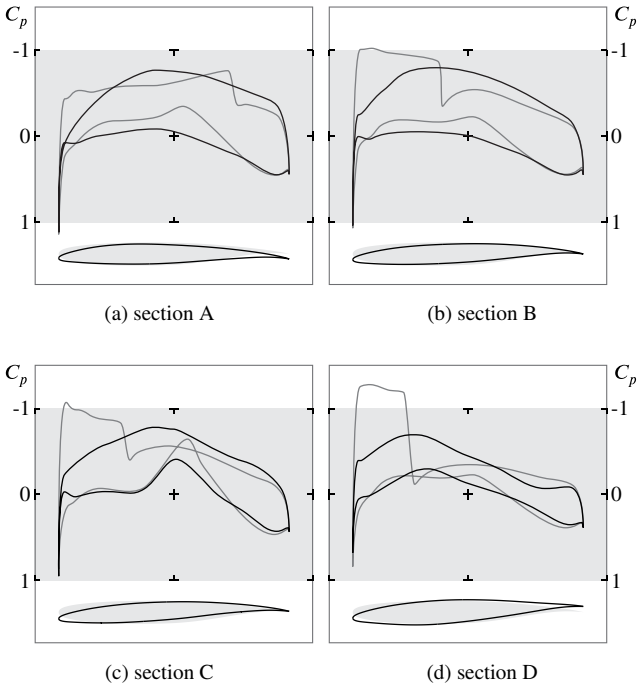

Fig. 14 Initial (gray) and optimized (black) pressure-coefficient profiles of the braced-wing configuration. Sections A–D correspond to those of Fig. 12a.

the vertical extent of the strut as much as it could, i.e. by maximizing the nozzle area.

It is worth noting that the downward force on the strut acted in favor of the trim constraint. Consequently, the optimizer did not contort the wing sections at the root as it did for the tube-and-wing. Still, as seen in Fig. 14, the final wing sections are substantially different from the initial ones.

IV. Conclusions

This paper presented the Euler-equation-based drag minimization of four distinct unconventional aircraft configurations targeted at the regional market segment. The same gradient-based optimization framework was used in each case in order to enable direct comparisons based on inviscid pressure drag. Relative to the baseline tube-and-wing, it was found that the box-wing, C-tip blended-wing-body, and braced-wing configurations investigated here produce respectively 34.1%, 36.2%, and 40.3% less induced drag.

The optimization results reinforced the realization that higher fidelity models than normally used are required for the investigation and assessment of unconventional aircraft configurations. Here the Euler equations proved to be accurate enough to not only capture but also exploit the nonlinear flow features of each configuration.

For the tube-and-wing, the optimizer morphed a winglet out of a planar wingtip extension without user intervention. It also applied significant side-forces to the winglet, in agreement with previous work stating that such forces are essential for diffusing the vortex at the tip. The final spanwise lift distribution is smooth and close to elliptical despite the side-forces experienced by the winglet and the small negative lift carried by the tail to trim the aircraft.

For the box wing, the optimizer reoriented the freestream angle of attack toward the out-of-plane axis of the front and rear wings, thus increasing their effective height-to-span ratio and span efficiency. It also adjusted the optimal force distribution to meet the trim constraint without any apparent drag penalty. This unique capability of the box-wing configuration to satisfy trim, stability, and possibly other requirements without penalizing induced drag largely compensates for its slight underperformance relative to other unconventional configurations of larger span such as the blended-wing-body and braced-wing configurations considered in this study.

For the blended wing-body, the optimizer shrunk the horizontal segment of the C-tip extension as much as it could, suggesting that when compressibility effects are accounted for a C-tip is not advantageous over a vertical winglet of the same height. Since compressibility effects reduce with increasing winglet height, it may be that this conclusion is unique to the configuration considered here.

For the braced wing, the optimizer easily satisfied the lift and trim constraints through minor twist and section shape changes. It also opted to generate a downward force on the strut in order to mitigate the nozzle effect in the wing-strut opening. However, by compensating with more lift on the wing, it still achieved an almost perfect overall elliptical lift distribution.

This study provides a unique perspective on the influence of flow nonlinearity on induced drag and the related implications for unconventional aircraft design. It does not, however, provide a definitive answer as to which unconventional aircraft is most promising. To help answer such questions it is imperative to also include the effects of viscosity and structures, among others, within the optimization problem. Such optimizations will be the focus of future research.

Acknowledgments

The authors are grateful for the financial support provided by the Governments of Quebec and Ontario, as well as the University of Toronto. Computations were performed on the General Purpose Cluster supercomputer at the SciNet High Performance Computing Consortium.

References

[1] Green, J. E., "Civil aviation and the environment – the next frontier for the aerodynamicist," *The Aeronautical Journal*, Vol. 110, No. 1110, 2006, pp. 469–486.

[2] Bushnell, D. M., "Frontier Aerospace Opportunities," Tech. Rep. TM-2014-218519, NASA, 2014.

[3] Kroo, I., "Nonplanar Wing Concepts for Increased Aircraft Efficiency," in Torenbeek, E. and Deconinck, H., eds., "Innovative configurations and advanced concepts for future civil transport aircraft," von Karman Institute, VKI Lecture Series, 2005.

[4] Munk, M. M., "The Minimum Induced Drag of Aerofoils," Tech. Rep. TR-121, NACA, 1923.

[5] Prandtl, L., "Induced Drag of Multiplanes," Tech. Rep. TN-182, NACA, 1924.

[6] Cone, C. D., "The Theory of Induced Lift and Minimum Induced Drag of Nonplanar Lifting Systems," Tech. Rep. TR-R-139, NASA, 1962.

[7] Blackwell, J. A., "Numerical Method to Calculate the Induced Drag or Optimum Loading for Arbitrary Non-Planar Aircraft," Tech. Rep. SP-405, NASA, 1976.

[8] Verstraeten, J. G. and Slingerland, R., "Drag Characteristics for Optimally Span-Loaded Planar, Wingletted, and C Wings," *Journal of Aircraft*, Vol. 46, No. 3, 2009, pp. 962–971, doi:10.2514/1.39426.

[9] Ning, S. A. and Kroo, I., "Multidisciplinary Considerations in the Design of Wings and Wing Tip Devices," *Journal of Aircraft*, Vol. 47, No. 2, 2010, pp. 534–543, doi:10.2514/1.41833.

[10] Jansen, P. W., Perez, R. E., and Martins, J. R. R. A., "Aerostructural Optimization of Nonplanar Lifting Surfaces," *Journal of Aircraft*, Vol. 47, No. 5, 2010, pp. 1490–1503, doi:10.2514/1.44727.

[11] Andrejašič, M. and Veble, G., "Shape Optimization of Nonplanar Lifting Surfaces and Planar-Nonplanar Break Points," *Journal of Aircraft*, Vol. 50, No. 3, 2013, pp. 798–806, doi:10.2514/1.C031991.

[12] Nguyen, N., Trinh, K., Reynolds, K., Kless, J., Aftosmis, M., Urnes, J., and Ippolito, C., "Elastically Shaped Wing Optimization and Aircraft Concept for Improved Cruise Efficiency," in "51st AIAA Aerospace Sciences Meeting

Including the New Horizons Forum and Aerospace Exposition," Grapevine, Texas, AIAA Paper 2013-0141, 2013, doi:10.2514/6.2013-141.

[13] van Dam, C. P., "Induced-drag characteristics of crescent-moon-shaped wings," *Journal of Aircraft*, Vol. 24, No. 2, 1987, pp. 115–119.

[14] Smith, S. C., "A Computational and Experimental Study of Nonlinear Aspects of Induced Drag," Tech. Rep. TP-3598, NASA, 1996.

[15] Smith, S. C. and Kroo, I. M., "Induced Drag Computations on Wings with Accurately Modeled Wakes," *Journal of Aircraft*, Vol. 34, No. 2, 1997, pp. 253–255, doi:10.2514/2.7570.

[16] Liersch, C. M., Streit, T., and Visser, K. D., "Numerical Implications of Spanwise Camber on Minimum Induced Drag Configurations," in "47th AIAA Aerospace Sciences Meeting Including The New Horizons Forum and Aerospace Exposition," Orlando, Florida, AIAA Paper 2009-898, 2009, doi:10.2514/6.2009-898.

[17] Werner-Westphal, C., Heinze, W., and Horst, P., "Multidisciplinary Integrated Preliminary Design Applied to Unconventional Aircraft Configurations," *Journal of Aircraft*, Vol. 45, No. 2, 2008, pp. 581–590, doi:10.2514/1.32138.

[18] La Rocca, G. and van Tooren, M. J. L., "Knowledge-Based Engineering Approach to Support Aircraft Multidisciplinary Design and Optimization," *Journal of Aircraft*, Vol. 46, No. 6, 2009, pp. 1875–1885, doi:10.2514/1.39028.

[19] Seywald, K., Hellmundt, F., Wildschek, A., and Holzapfel, F., "Airworthiness Investigation of a Highly Nonplanar Flexible Wing Concept," in "29th Congress of International Council of the Aeronautical Sciences," Saint Petersburg, Russia, Paper ICAS2014_0088, 2014.

[20] Vassberg, J. C. and Jameson, A., "Theoretical Background for Aerodynamic Shape Optimization," in Périaux, J. and Verstraete, T., eds., "Introduction to optimization and multidisciplinary design in aeronautics and turbomachinery," von Karman Institute, VKI Lecture Series, 2014.

[21] Makino, Y., Iwamiya, T., and Lei, Z., "Fuselage Shape Optimization of a Wing-Body Configuration with Nacelles," *Journal of Aircraft*, Vol. 40, No. 2, 2003, pp. 297–302, doi:10.2514/2.3093.

[22] Koc, S., Kim, H.-J., and Nakahashi, K., "Aerodynamic Design of Complex Configurations with Junctions," *Journal of Aircraft*, Vol. 43, No. 6, 2006, pp. 1838–1844, doi:10.2514/1.20723.

[23] Hicken, J. E. and Zingg, D. W., "Induced-Drag Minimization of Nonplanar Geometries Based on the Euler Equa-

tions," *AIAA Journal*, Vol. 48, No. 11, 2010, pp. 2564–2575,
doi:10.2514/1.J050379.

[24] Leung, T. M. and Zingg, D. W., "Aerodynamic Shape Optimization of Wings Using a Parallel Newton-Krylov Approach," *AIAA Journal*, Vol. 50, No. 3, 2012, pp. 540–550,
doi:10.2514/1.J051192.

[25] Schmidt, S., Ilic, C., Schulz, V., and Gauger, N. R., "Three-Dimensional Large-Scale Aerodynamic Shape Optimization Based on Shape Calculus," *AIAA Journal*, Vol. 51, No. 11, 2013, pp. 2615–2627,
doi:10.2514/1.J052245.

[26] Takenaka, K., Hatanaka, K., Yamazaki, W., and Nakahashi, K., "Multidisciplinary Design Exploration for a Winglet," *Journal of Aircraft*, Vol. 45, No. 5, 2008, pp. 1601–1611,
doi:10.2514/1.33031.

[27] Kenway, G. K. W. and Martins, J. R. R. A., "Multipoint High-Fidelity Aerostructural Optimization of a Transport Aircraft Configuration," *Journal of Aircraft*, Vol. 51, No. 1, 2014, pp. 144–160,
doi:10.2514/1.C032150.

[28] Khosravi, S. and Zingg, D. W., "A Numerical Optimization Study on Winglets," in "15th AIAA/ISSMO Multidisciplinary Analysis and Optimization Conference," Atlanta, Georgia, AIAA Paper 2014-2173, 2014,
doi:10.2514/6.2014-2173.

[29] Lange, R. H., "Review of unconventional aircraft design concepts," *Journal of Aircraft*, Vol. 25, No. 5, 1988, pp. 385–392,
doi:10.2514/3.45592.

[30] Drela, M., "Development of the D8 Transport Configuration," in "29th AIAA Applied Aerodynamics Conference," Honolulu, Hawaii, AIAA Paper 2011-3970, 2011,
doi:10.2514/6.2011-3970.

[31] Whitcomb, R. T., "Review of NASA supercritical airfoils," in "9th Congress of the International Council of the Aeronautical Sciences," Haifa, Isreal, 1974.

[32] Gagnon, H. and Zingg, D. W., "Geometry Generation of Complex Unconventional Aircraft with Application to High-Fidelity Aerodynamic Shape Optimization," in "21st AIAA Computational Fluid Dynamics Conference," San Diego, California, AIAA Paper 2013-2850, 2013,
doi:10.2514/6.2013-2850.

[33] Raymer, D. P., *Aircraft Design: A Conceptual Approach*, AIAA Education Series, AIAA, Reston, 5th ed., 2012.

[34] Lange, R. H., Cahill, J. F., Bradley, E. S., Eudaily, R. R., Jenness, C. M., and MacWilkinson, D. G., "Feasibility study of the transonic biplane concept for transport aircraft application," Tech. Rep. NASA-CR-132462, Lockheed-

Georgia Company, 1974.

[35] Frediani, A., "The Prandtl wing," in Torenbeek, E. and Deconinck, H., eds., "Innovative configurations and advanced concepts for future civil transport aircraft," von Karman Institute, VKI Lecture Series, 2005.

[36] Addoms, R. B. and Spaid, F. W., "Aerodynamic Design of High-Performance Biplane Wings," *Journal of Aircraft*, Vol. 12, No. 8, 1975, pp. 629–630,
doi:10.2514/3.59846.

[37] Qin, N., Vavalle, A., Le Moigne, A., Laban, M., Hackett, K., and Weinerfelt, P., "Aerodynamic considerations of blended wing body aircraft," *Progress in Aerospace Sciences*, Vol. 40, No. 6, 2004, pp. 321–343,
doi:10.1016/j.paerosci.2004.08.001.

[38] Peigin, S. and Epstein, B., "Computational Fluid Dynamics Driven Optimization of Blended Wing Body Aircraft," *AIAA Journal*, Vol. 44, No. 11, 2006, pp. 2736–2745,
doi:10.2514/1.19757.

[39] Hileman, J. I., Spakovszky, Z., Drela, M., Sargeant, M. A., and Jones, A., "Airframe Design for Silent Fuel-Efficient Aircraft," *Journal of Aircraft*, Vol. 47, No. 3, 2010, pp. 956–969,
doi:10.2514/1.46545.

[40] Lyu, Z. and Martins, J. R. R. A., "Aerodynamic Design Optimization Studies of a Blended-Wing-Body Aircraft," *Journal of Aircraft*, Vol. 51, No. 5, 2014, pp. 1604–1617,
doi:10.2514/1.C032491.

[41] Reist, T. A. and Zingg, D. W., "Optimization of the Aerodynamic Performance of Regional and Wide-Body-Class Blended Wing-Body Aircraft," in "33rd AIAA Applied Aerodynamics Conference," Dallas, Texas, AIAA Paper 2015-3292, 2015,
doi:10.2514/6.2015-3292.

[42] McMasters, J. H. and Kroo, I. M., "Advanced configurations for very large transport airplanes," *Aircraft Design*, Vol. 1, No. 4, 1998, pp. 217–242,
doi:10.1016/S1369-8869(98)00018-4.

[43] Liebeck, R. H., "Design of the Blended Wing Body Subsonic Transport," *Journal of Aircraft*, Vol. 41, No. 1, 2004, pp. 10–25,
doi:10.2514/1.9084.

[44] Pfenninger, W., "Design Considerations of Large Global Range High Subsonic Speed LFC Transport Airplanes," Tech. Rep. R-654, AGARD, 1977.

[45] Gundlach, J. F., Tétrault, P.-A., Gern, F. H., Nagshineh-Pour, A. H., Ko, A., Schetz, J. A., Mason, W. H., Kapania, R. K., Grossman, B., and Haftka, R. T., "Conceptual Design Studies of a Strut-Braced Wing Transonic Transport,"

Journal of Aircraft, Vol. 37, No. 6, 2000, pp. 976–983,
doi:10.2514/2.2724.

[46] Gern, F. H., Naghshineh-Pour, A. H., Sulaeman, E., Kapania, R. K., and Haftka, R. T., "Structural Wing Sizing for Multidisciplinary Design Optimization of a Strut-Braced Wing," *Journal of Aircraft*, Vol. 38, No. 1, 2001, pp. 154–163,
doi:10.2514/2.2747.

[47] Gur, O., Schetz, J. A., and Mason, W. H., "Aerodynamic Considerations in the Design of Truss-Braced-Wing Aircraft," *Journal of Aircraft*, Vol. 48, No. 3, 2011, pp. 919–939,
doi:10.2514/1.C031171.

[48] Bhatia, M., Kapania, R. K., and Haftka, R. T., "Structural and Aeroelastic Characteristics of Truss-Braced Wings: A Parametric Study," *Journal of Aircraft*, Vol. 49, No. 1, 2012, pp. 302–310,
doi:10.2514/1.C031556.

[49] Bradley, M. K. and Droney, C. K., "Subsonic Ultra Green Aircraft Research Phase II: N+4 Advanced Concept Development," Tech. Rep. NASA/CR-2012-217556, Boeing Research and Technology, 2012.

[50] Carrier, G., Atinault, O., Dequand, S., Hantrais-Gervois, J.-L., Liauzun, C., Paluch, B., Rodde, A.-M., and Toussaint, C., "Investigation of a Strut-Braced Wing Configuration for Future Commercial Transport," in "28th Congress of the International Council of the Aeronautical Sciences," Brisbane, Australia, Paper ICAS 2012-1.10.2, 2012.

[51] Hicken, J. E. and Zingg, D. W., "Aerodynamic Optimization Algorithm with Integrated Geometry Parameterization and Mesh Movement," *AIAA Journal*, Vol. 48, No. 2, 2010, pp. 400–413,
doi:10.2514/1.44033.

[52] Gagnon, H. and Zingg, D. W., "Two-Level Free-Form and Axial Deformation for Exploratory Aerodynamic Shape Optimization," *AIAA Journal*, Vol. 53, No. 7, 2015, pp. 2015–2026,
doi:10.2514/1.J053575.

[53] van Dam, C. P., Nikfetrat, K., Wong, K., and Vijgen, P. M. H. W., "Drag prediction at subsonic and transonic speeds using Euler methods," *Journal of Aircraft*, Vol. 32, No. 4, 1995, pp. 839–845,
doi:10.2514/3.46799.

[54] Yamazaki, W., Matsushima, K., and Nakahashi, K., "Aerodynamic Design Optimization Using the Drag-Decomposition Method," *AIAA Journal*, Vol. 46, No. 5, 2008, pp. 1096–1106,
doi:10.2514/1.30342.

[55] Chernukhin, O., , and Zingg, D. W., "Multimodality and Global Optimization in Aerodynamic Design," *AIAA Journal*, Vol. 51, No. 6, 2013, pp. 1342–1354,
doi:10.2514/1.J051835.

[56] Osusky, L., Buckley, H., Reist, T., and Zingg, D. W., "Drag Minimization Based on the Navier-Stokes Equations Using a Newton-Krylov Approach," *AIAA Journal*, Vol. 53, No. 6, 2015, pp. 1555–1577, doi:10.2514/1.J053457.

[57] Whitcomb, R. T., "A Design Approach and Selected Wind-Tunnel Results at High Subsonic Speeds for Wing-Tip Mounted Winglets," Tech. Rep. TN-D-8260, NASA, 1976.

[58] Gagnon, H. and Zingg, D. W., "Aerodynamic Optimization Trade Study of a Box-Wing Aircraft Configuration," *Journal of Aircraft* (accepted), doi:10.2514/1.C033592.

[59] Wolkovitch, J., "The joined wing: An overview," *Journal of Aircraft*, Vol. 23, No. 3, 1986, pp. 161–178, doi:10.2514/3.45285.

[60] Cerón-Muñoz, H. D., Diaz-Izquierdo, D. O., Solarte-Pineda, J., and Catalano, F. M., "Aerodynamic Interference of Wingtip and Wing Devices on BWB Model," in "29th Congress of International Council of the Aeronautical Sciences," Saint Petersburg, Russia, Paper ICAS2014_0933, 2014.

[61] Demasi, L., Dipace, A., Monegato, G., and Cavallaro, R., "Invariant Formulation for the Minimum Induced Drag Conditions of Nonplanar Wing Systems," *AIAA Journal*, Vol. 52, No. 10, 2014, pp. 2223–2240, doi:10.2514/1.J052837.

[62] Ko, A., Mason, W. H., and Grossman, B., "Transonic Aerodynamics of a Wing/Pylon/Strut Juncture," in "21st AIAA Applied Aerodynamics Conference," Orlando, Florida, AIAA Paper 2003-4062, 2003, doi:10.2514/6.2003-4062.